Ultrasonic Determination of Mechanical Moduli of Oriented Semicrystalline Polymers

DANIEL LÉVESQUE, NATHALIE LEGROS, *and* ABDELLAH AJJI

Industrial Materials Institute, National Research Council Canada
Boucherville, Québec, Canada J4B 6Y4

Ultrasonics has been used for the determination of the mechanical properties of oriented semicrystalline polymers through time-of-flight measurements of elastic waves propagating in various directions within the material. While being nondestructive, such a method allows one to obtain more mechanical moduli with a better accuracy than the conventional tensile tests, especially regarding the shear properties and the Poisson's coefficients. Until now, the approach used to interpret the data was approximate and not rigorous. We present here a self-consistent rigorous approach for interpreting time-of-flight data based on the group velocity including allowance for lateral displacement of the transmitted beam. Results are presented for roll-drawn PET with various draw ratios. These samples are considered to have transversely isotropic symmetry. For the Young's moduli, comparisons are made with conventional tensile tests and the differences observed are interpreted in terms of viscoelastic effects considering both the amorphous and crystalline phases.

1. INTRODUCTION

One approach for the production of polymers with high mechanical performance consists in orienting the chain structures by drawing or extrusion in the solid state. When an unoriented, isotropic, sheet of polymer material is oriented, it becomes elastically anisotropic due to orientation of molecular chains. Several techniques have been developed to assess orientation at the microscopic level namely, optical birefringence, X-rays, laser Raman spectroscopy and polarized infrared techniques (1). While being important in fundamental studies in order to identify the mechanisms involved, these methods have several drawbacks: they do not yield directly mechanical properties and/or require expensive or complex instrumentation. There is a great need for better adapted testing procedures and, in particular, for nondestructive methods.

For this purpose, an ultrasonic technique has been developed and applied for characterizing orientation and evaluating the different components of stiffness properties (2, 3). The method consists in measuring the time of flight of elastic waves that propagate in various directions within the material. By making a sufficient number of measurements for different propagation directions, it is possible to determine the different stiffness components. While being nondestructive, such a method allows one to obtain more mechanical moduli with better accuracy than using conventional tensile tests, especially regarding the moduli related to shear properties (4). However, a detailed mapping of mechanical anisotropy and the computation of stiffness constants are quite involved and require a nonlinear least-square fit of the data to the predictions of a model for wave propagation. Although the procedure has been well developed and applied successfully to various anisotropic materials such as oriented polymers (3) and fiber reinforced composites (5), several difficulties still remain (6).

The first is related to the interpretation of time-of-flight data whether the technique used is water immersion or direct contact method or laser-generated ultrasound. Until recently, most reported works neglected the fact that time-of-flight measurements are related indeed to the group velocity (energy flux) while using at the same time a formalism based on phase velocity (wave front). Since these velocities in general deviate from each other in anisotropic materials, the use of a model based on phase velocity to determine the elastic constants raises serious questions about the correctness of the technique. When this fact is properly accounted, a tedious procedure implying numerical derivatives with respect to the wave normals is used (7, 8). For water immersion only, it was demonstrated (4) that the time of flight associated with the energy flux (i.e. to the group velocity) is equivalent to the one linked to the undetectable wave front (i.e. to the phase velocity) emerging at a different point, provided that an appropriate reference path be chosen. Such an equivalence is certainly not possible with the above other techniques. Since in a recent paper (9), closed-form analytical relations were derived for group velocity, there is no reason to rely on an approximate model for the determination of the elastic constants and a more rigorous approach is readily feasible.

A second difficulty associated with the immersion technique is the proper handling of the lateral displacement of the transmitted beam. It appears natural to follow this displacement by moving the receiving transducer to capture the maximum energy. Actually, when this is neglected and the transducer is fixed, an error is made on the time of flight measurement. This may result in an underestimation of some elastic constants attaining 30% for the axial Young's modulus. With oriented polymers, this underestimation may yield to an apparent good agreement between ultrasonic and tensile measurements, which is suspicious since high frequency ultrasound should give higher modulus according to the time-temperature equivalence principle of viscoelasticity. Recognizing the importance of beam displacement and circumventing the task of following the beam, a double-through-transmission method has been proposed (4) and is based on the reciprocity of wave propagation. However, this approach is less useful for roll-drawn oriented polymers since the two faces have to be precisely parallel. The wave amplitude is also quite reduced after double propagation in the case of strongly attenuating materials. The displacement of the beam is therefore an important factor that is analyzed and properly taken into account in this paper. Finally, still another concern addressed in this paper is the robustness of the algorithm to recover the stiffness constants from the time-of-flight data (6, 10).

We present a self-consistent approach based on group velocity formalism for analyzing time-of-flight data. The formalism takes into account the lateral displacement of the transmitted beam and the receiving transducer. We present also a robust algorithm for the recovery of elastic constants from the time-of-flight data. Results are presented for the roll-drawing of a semicrystalline poly(ethylene terephthalate) (PET) in the solid state of various draw ratios. For the Young's moduli, comparisons are made with tensile tests and the interpretation for the differences is given in terms of the time-temperature equivalence principle of viscoelasticity considering both the amorphous and crystalline phases.

2. THEORY OF ANISOTROPY

Phase and Group Velocities

Basically, ultrasonics involves the reverberation of a short ultrasonic pulse propagating in the materials from which times of flight or delays between pulses can be measured. For the simple case of isotropic materials, knowledge of the sample thickness allows one to obtain the velocity, v, of the wave and the elastic modulus, M, is deduced from the relation $M = \rho v^2$, where ρ is the density. This can be made for both longitudinal and transverse waves and yield the two independent constants characterizing the isotropic material. The derivation of the elastic moduli from the time-of-flight measurements for anisotropic materials such as oriented polymers is, however, more involved.

Let us first consider the geometry in *Fig. 1*, with the axis 3 in the draw direction. In general, components of the stiffness tensor are made of 21 independent elastic constants but this number is greatly reduced when there are some symmetries in the material (11). The case of thin slabs or biaxial orientation by drawing require 9 independent stiffness constants, corresponding to orthotropic symmetry. The relation between phase velocities v_p and elastic constants of the material is given by the Christoffel equation:

$$|\Gamma_{ik} - \rho v_p^2 \delta_{ik}| = 0 \tag{1}$$

where δ_{ik} is the Kronecker delta, ρ is the density of the material and components Γ_{ik} for the orthotropic symmetry are (9, 12):

$$\begin{aligned}
\Gamma_{11} &= n_1^2 C_{11} + n_2^2 C_{66} + n_3^2 C_{55} \\
\Gamma_{22} &= n_1^2 C_{66} + n_2^2 C_{22} + n_3^2 C_{44} \\
\Gamma_{33} &= n_1^2 C_{55} + n_2^2 C_{44} + n_3^2 C_{33} \\
\Gamma_{23} &= n_2 n_3 (C_{23} + C_{44}) \\
\Gamma_{13} &= n_1 n_3 (C_{13} + C_{55}) \\
\Gamma_{12} &= n_1 n_2 (C_{12} + C_{66})
\end{aligned} \tag{2}$$

with C_{IJ}, the components of the stiffness tensor (using collapsed indices $I \equiv ij$ and $J \equiv kl$) and the n_i, the direction cosines of the normal to the wave front. For

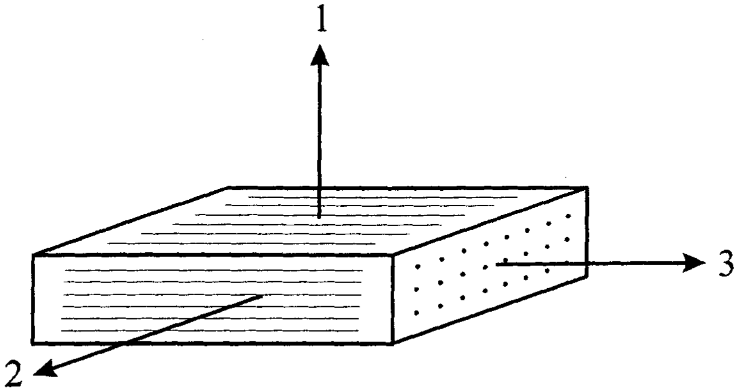

Fig. 1. Geometry used for an anisotropic material.

an arbitrary direction in the material, the cubic polynomial in v_p^2 indicates that in general, three modes can propagate: a quasi-longitudinal wave (QL mode), a quasi-transverse wave (QS mode) and a pure transverse wave (PT mode). Here, the plate is considered to be isotropic in the plane perpendicular to drawing, whereby only five stiffness constants are needed corresponding to transversely isotropic symmetry. In any case, different measurements in the transverse plane will allow direct validation of the approximation. For that symmetry, the following relations hold:

$$
\begin{aligned}
C_{22} &= C_{11} \\
C_{55} &= C_{44} \\
C_{23} &= C_{13} \\
C_{12} &= C_{11} - 2C_{66} \qquad (3)
\end{aligned}
$$

In principle, phase velocity measurements in different directions of the material with the requirement that *Eqs 1–3* must be satisfied would allow to determine the independent components of the stiffness matrix C_{IJ}.

Once the five stiffness components are known, seven engineering constants usually measured by static methods can be obtained. Primarily defined in terms of the compliance matrix $S_{IJ} \equiv [C_{IJ}]^{-1}$, these constants are (1, 12): the axial and transverse Young moduli:

$$E_3 \equiv \frac{1}{S_{33}} = \frac{C}{C_{11}^2 - C_{12}^2}$$

$$E_1 \equiv \frac{1}{S_{11}} = \frac{C}{C_{33}C_{11} - C_{13}^2}$$

$$C = (C_{11} - C_{12})[C_{33}(C_{11} + C_{12}) - 2C_{13}^2] \qquad (4)$$

the shear moduli:

$$G_{13} \equiv \frac{1}{S_{44}} = C_{44} = G_{23}$$

$$G_{12} \equiv \frac{1}{S_{66}} = C_{66} \qquad (5)$$

and Poisson's ratios:

$$\nu_{13} \equiv -\frac{S_{13}}{S_{33}} = \frac{C_{13}}{C_{11} + C_{12}} = \nu_{23}$$

$$\nu_{12} \equiv -\frac{S_{12}}{S_{22}} = \frac{C_{33}C_{12} - C_{13}^2}{C_{33}C_{11} - C_{13}^2} = \nu_{21}$$

$$\nu_{31} \equiv -\frac{S_{31}}{S_{11}} = \frac{(C_{11} - C_{12})C_{13}}{C_{33}C_{11} - C_{13}^2} = \nu_{32} \qquad (6)$$

In order to determine the stiffness components from time-of-flight measurements, different approaches can be envisaged that have incidence on the n_j's in *Eq 2*. The simplest approach is to propagate waves in symmetry planes 1–2 and 1–3. For propagation in the isotropic plane 1–2, appropriate n_j's in *Eq 2* yield the simple equations:

$$v_p^{QL} = \sqrt{\frac{C_{11}}{\rho}} \qquad v_p^{QS} = \sqrt{\frac{C_{66}}{\rho}} \qquad v_p^{PT} = \sqrt{\frac{C_{44}}{\rho}} \qquad (7)$$

relating phase velocities to the elastic constants and being independent of the angle with respect to axis 1. For propagation in the anisotropic plane 1–3, *Eq 2* yields the expressions (8, 9):

$$v_p^{QL,QS} = \sqrt{\frac{a \pm b}{2\rho}} \qquad v_p^{PT} = \sqrt{\frac{d}{\rho}} \qquad (8)$$

the upper and lower signs being, respectively, for QL and QS waves, with:

$$
\begin{aligned}
a &= C_{11+}\cos^2\theta_p + C_{33+}\sin^2\theta_p \\
b &= [(C_{11-}\cos^2\theta_p - C_{33-}\sin^2\theta_p)^2 \\
&\qquad + (2C_{13+}\cos\theta_p\sin\theta_p)^2]^{1/2} \qquad (9) \\
d &= C_{66}\cos^2\theta_p + C_{44}\sin^2\theta_p
\end{aligned}
$$

$$
\begin{aligned}
C_{11\pm} &= C_{11} \pm C_{44} \\
C_{33\pm} &= C_{33} \pm C_{44} \\
C_{13+} &= C_{13} + C_{44}
\end{aligned}
$$

and where the angle θ_p is the wave propagation direction with respect to the axis 1. Given the elastic properties, phase velocities of all three modes are easily determined for a given direction θ_p.

However, it is well known that the wave propagation direction does not generally coincide with the direction of energy flux for anisotropic media, and also that their respective beams do not propagate with the same velocity. This is of importance considering the fact that indeed, the apparatus involved with ultrasonic techniques is more likely sensitive to energy flux than to the wave front. The wave front has the phase velocity v_p as already discussed and the energy flux propagates with the so-called group velocity v_g. For any three modes QL, QS, and PT, the phase velocity can be seen as the projection of the group velocity onto the direction of wave propagation. Defining the paths of wave front and energy flux in reference to axis 1 with angles θ_p, θ_g, respectively, we have the relation (12):

$$v_p = v_g\cos(\theta_g - \theta_p) \qquad (10)$$

It should be noted that since we are only considering propagation in symmetry planes both paths are located in the incidence plane. For the transversely isotropic case of propagation in the plane 1–2, propagation of the wave front and energy flux coincide and the distinction has to be made only in the anisotropic plane 1–3. In this plane, wave front and energy flux coincide however for propagation along principal axes 1 and 3.

If an additional relation involving θ_g exists, *Eq 10* could be used to relate ultrasonic velocity measurements to phase velocities given by *Eqs 8, 9*. However, until very recently, no such analytical relation was available. Most workers in the field neglected the problem, and those who didn't relied on a tedious procedure that implies numerical derivatives with respect to the n_j's (7, 8). In a recent paper (9), closed-form analytical relations were given for θ_g and v_g in terms of the stiffness constants. In replacement of *Eqs 8, 9*, these expressions are:

$$v_g^{QL,QS} = \sqrt{\frac{[C_{33-}^2\sin^2\theta_p - (C_{11-}^2 \pm 2bC_{11+})\cos^2\theta_p - b^2]^2}{8\rho b^2\cos^2\theta_p\cos^2\theta_g(a \pm b)}} \qquad (11)$$

where

$$\tan\,\theta_g = \tan\,\theta_p \cdot \frac{(C_{11-}C_{33-} - 2C_{13+}^2)\cos^2\theta_p - C_{33-}^2\sin^2\theta_p \mp C_{33+}b}{(C_{11-}C_{33-} - 2C_{13+}^2)\sin^2\theta_p - C_{11-}^2\cos^2\theta_p \mp C_{11+}b} \qquad (12)$$

with *a* and *b* taken from *Eq 9* and the upper and lower signs being, respectively, for QL and QS waves. One notices that the correspondence between v_g and θ_g is not straightforward, but rather made through the wave front angle θ_p. On the contrary, the relation between v_g and θ_g for the PT wave is simply:

$$v_g^{PT} = \sqrt{\frac{C_{66}C_{44}}{\rho(C_{66}\sin^2\theta_g + C_{44}\cos^2\theta_g)}} \qquad (13)$$

with the angle θ_p related to θ_g by:

$$\tan\,\theta_g = \tan\,\theta_p\left(\frac{C_{44}}{C_{66}}\right) \qquad (14)$$

Therefore given the elastic properties, group velocities of all three modes are determined for a given direction θ_g.

Representation of Anisotropy

For symmetry planes 1–2 and 1–3, anisotropy properties of the material can be shown using a representation based on velocities in all directions. For the purpose of illustration, phase or group velocities will be shown assuming typical properties for oriented polymer materials, as given in *Table 1*. As discussed in the next section, an immersion technique will be used and therefore, propagation of shear waves in the materials will be effective through mode conversion that occurs at the sample surface. However, mode PT, which is polarized perpendicularly to the plane of incidence, cannot be excited by mode conversion. Therefore, in the remainder, only L ≡ QL and S ≡ QS modes will be considered. Provided measurements are made in both planes 1–2 and 1–3, a complete characterization will be possible since all five stiffness constants are involved for these two modes (see *Eqs 7–12*).

Table 1. Set of Physical Properties Used for Calculation in the Example.

Properties	Values
Density	970 kg/m^3
C_{11}	5 GPa
C_{33}	15 GPa
C_{44}	1.0 GPa
C_{66}	1.5 GPa
C_{13}	3 GPa

For the set of properties in *Table 1*, *Fig. 2* shows the representation for phase velocity v_p. The four curves are labeled for the mode (L or S) and the symmetry plane (1–2 or 1–3) and plotted values are inverse of velocity, that is slowness $s_p \equiv 1/v_p$, but normalized with the acoustic velocity in water v_w = 1485 m/s. Such a figure should not be interpreted in terms of an *x–y* graph but more like a polar plot. Therefore, the horizontal axis corresponds to angle direction $\theta_p = 0°$ and principal axis 1 while the vertical axis corresponds to $\theta_p = 90°$ and either principal axis 2 or 3 depending on symmetry plane. For a given angle θ_p lying between 0° and 90°, the length of the joining vector from the origin to the corresponding point in the curve gives the slowness value s_p for the chosen mode and symmetry plane. Three reasons can be given for using slownesses instead of velocities: 1) propagation models naturally involve the wavenumber $k = \omega/v_p$, 2) simultaneously representing L and S waves, emphasis is made on the more complicated behavior associated with S-wave (lower velocity) and consequently, 3) least-square fits for extracting elastic constants from slownesses should be more stable.

For plane 1–2, the circular patterns indicate that phase velocities for L and S modes are constants, therefore corresponding to transversely isotropic symmetry. For plane 1–3 and L mode, slowness at $\theta_p = 0°$ has the same value as for plane 1–2 and decreases upon reaching $\theta_p = 90°$ or principal axis 3, in relation with a velocity that increases with higher modulus. For the S mode, a more complicated behavior is ob-

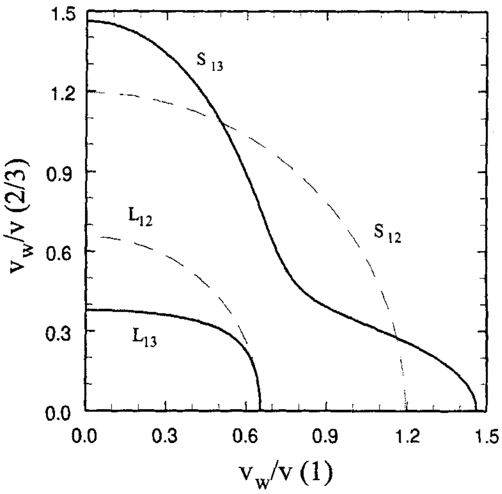

Fig. 2. Polar plot of slowness $s_p = 1/v_p$ vs θ_p for L and S modes in symmetry planes 1–2 and 1–3 using the set of properties in Table 1.

served, and, in contrast to L mode, the value at $\theta_p = 0°$ is different from the one in plane 1-2. This can be expected since they actually correspond to different polarizations.

Now, using *Eq 12* with the data of *Table 1* for symmetry plane 1-3, we compute the direction of energy θ_g as a function of wave front direction θ_p, and this is shown in *Fig. 3*. One can observe a large effect, except for the principal axes 1 and 3 corresponding to $\theta_p = 0°$ and 90°, for which wave front and energy flux directions coincide. The departures attain 35° for L waves and 50° for S waves and a crossover is observed for S wave near $\theta_p = 35°$. Moreover, the sigmoid behavior for the S wave is indicative of a so-called cuspidal region in the material with an angular range θ_g between 20° and 65°. That is, an ultrasonic beam within this range of angles may correspond to any of three different wave front directions.

Such a region is more readily observed in the slowness representation of *Fig. 4*, which shows the polar plot representation for group velocity v_g as a function of the angle θ_g for the given set of properties in *Table 1*. Here again, the four curves are labeled for the mode (L or S) and the symmetry plane (1-2 or 1-3). The length of the joining vector from origin to a point on a given curve indicates the slowness $s_g \equiv 1/v_g$, normalized to the acoustic velocity in water. Behavior for group velocity shown in *Fig. 4* is typical of what should be observed with the ultrasonic beam in oriented polymers. As noted for the isotropic plane 1-2, the circular patterns indicate that the velocities for the L and S modes are constant. For the plane 1-3 and L mode, slowness at $\theta_g = 0°$ has the same value as for plane 1-2 and decreases (velocity increases) upon reaching $\theta_g = 90°$ or principal axis 3. For the S mode, a more complicated behavior is observed, and one notices the cuspidal region as already discussed, for θ_g lying between 20° and 65°. That is, energy flux propagating in a given direction within that range possesses a group velocity which is different depending on which one of the two or three wave fronts it is associated with.

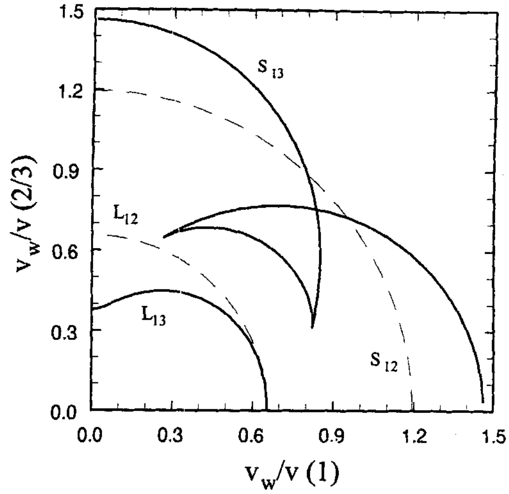

Fig. 4. Polar plot of slowness $s_g = 1/v_g$ vs θ_g for L and S modes in symmetry planes 1-2 and 1-3 using the set of properties in Table 1.

Using an immersion technique, this multiplicity of roots for a given direction of energy is somewhat eliminated since the wave front direction in the material is connected with incident beam by the Snell-Descartes law. Therefore, a convenient way of representing the group velocity is shown in *Fig. 5* for the given set of properties in *Table 1*. Instead of using the angle θ_g in this *Figure*, the mapping of slowness $s_g \equiv 1/v_g$ associated with energy is made with the corresponding wave front direction θ_p. Here again, the four curves are normalized with the acoustic velocity in water and labeled as before. For a direction θ_p, *Fig. 5* allows one to obtain the group velocity of the energy, but propagating in a direction θ_g given by *Fig. 3*.

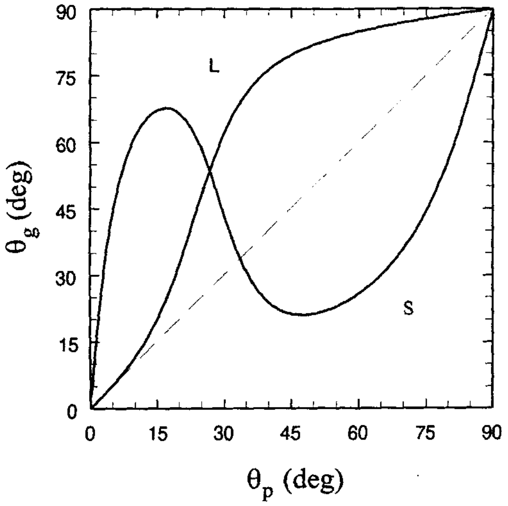

Fig. 3. Direction of the beam energy θ_g as a function of wave front direction θ_p for both L and S waves in symmetry plane 1-3.

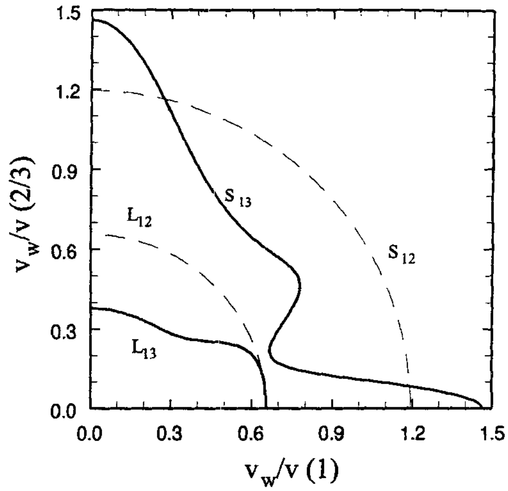

Fig. 5. Polar plot of slowness $s_g = 1/v_g$ vs θ_p for L and S modes in symmetry planes 1-2 and 1-3 using the set of properties in Table 1.

3. ULTRASONIC TECHNIQUE

Immersion Technique and Data Analysis

The generation/detection of an ultrasonic wave in a material may be accomplished in different ways by direct contact, water immersion, and laser generation/detection. We are using here an immersion technique, whereby the transducers and the sample are submerged in water, acting as the coupling medium for ultrasound.

In *Fig. 6*, the water immersion tank is shown with the sample placed on a turntable that can change its orientation with respect to the ultrasonic beam. Hence, measurements can be made at different angles θ_w in either symmetry plane 1–2 or 1–3. By application of Snell's law, this arrangement permits the generation of both longitudinal and shear waves in the sample. By making a sufficient number of time-of-flight measurements over various orientations, one may determine the stiffness constants. The transducer T used for insonification produces a pulse of 3 MHz center frequency with a flat profile of diameter 1 cm, aligned with the center line of the sample. The transducer R, similar to T and used for detection of the signal, is also allowed to move laterally, i.e. along a direction perpendicular to the line of insonification. As mentioned previously, this is to follow the path of the acoustic beam. The signals received are digitized at a 100 MHz sampling rate and then averaged 10 times. The temperature in the bath is monitored and controlled with variations smaller than ±5°C, making the sound velocity in water to vary between 1480 and 1490 m/s. Therefore, a fixed value v_w = 1485 m/s is adopted for use in the calculations with an error of less than 0.4%. The method is estimated to be reliable for samples of flat profiles with thickness in the range from 1 to 15 mm to ensure sufficient separation of echoes.

Similarly to the propagation of light, when the wave is incident at an angle θ_w on a surface, part of the wave is reflected away from the surface and part is refracted inside the second medium. But the difference with optics is that oblique incidence, $\theta_w \neq 0$, gives rise to mode conversion. As illustrated in *Fig. 7*, starting with an L wave (the only mode permitted in water), the presence of an interface produces an L wave and an S wave propagating in the second medium with different directions. For a slab with parallel faces, part of both wave modes are reflected at the second interface and part is transmitted (after conversion for the S wave) into an L wave in water. Only for that geometry, both outgoing beams are parallel to the incident one, but as already mentioned, transducer R has to be moved laterally to follow the path of respective beams. Snell's law of optics can still be used to obtain a relation between incident wave and wave front (phase) of both L and S modes propagating in the material. The expressions are:

$$\sin\theta_w = \sin\theta_p^L\left(\frac{v_w}{v_p^L}\right)$$

$$\sin\theta_w = \sin\theta_p^S\left(\frac{v_w}{v_p^S}\right) \qquad (15)$$

In view of *Eq 15*, two remarks can be made. First, when $v_w < v_p$ as the case for L waves on either symmetry plane of the example, the whole range of prop-

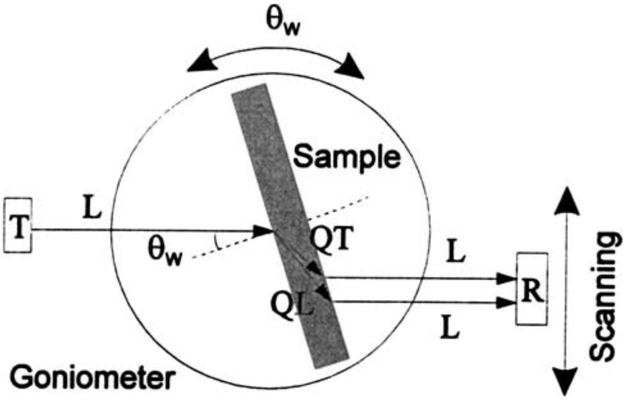

Fig. 6. Schematic diagram of the ultrasonic experiment: top view of transducers T and R together with the sample immersed in water. The sample may be rotated for insonification at different angles θ_w.

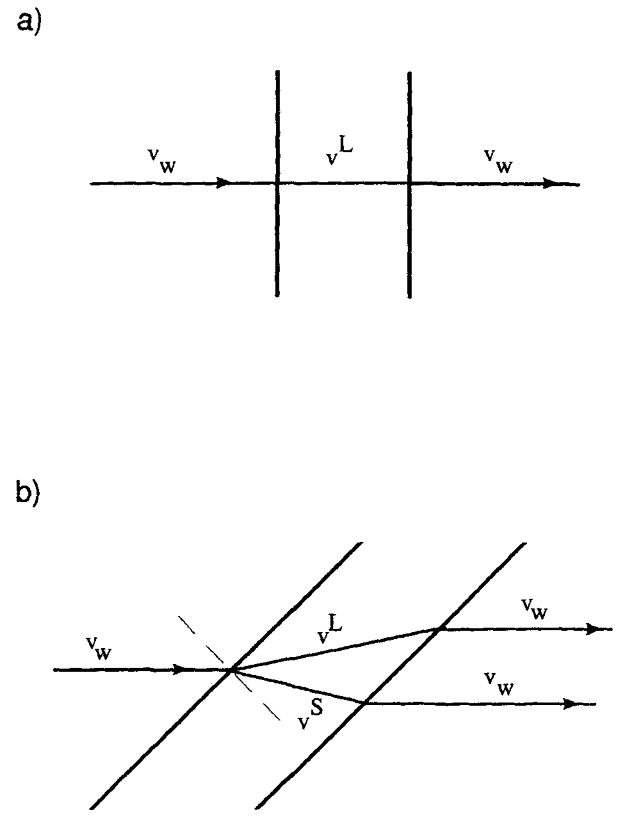

Fig. 7. The concept of mode conversion and refraction by Snell's law for ultrasonic waves: a) normal incidence and b) oblique incidence.

agation angles in the materials $0° \le \theta_p \le 90°$ is easily achieved using an immersion technique with:

$$0 \le \theta_w < \sin^{-1}\left(\frac{v_w}{v_p}\right) \tag{16}$$

Second, when $v_w \ge v_p$ as for S waves, measurements over the whole range $0° \le \theta_w \le 90°$ allow one to span only a portion of the slowness curves. The right-hand side of *Eq 15* restricted to be <1.0, the range of propagation angle in the materials is given by:

$$0 < \theta_p \le \sin^{-1}\left(\frac{v_p}{v_w}\right) \tag{17}$$

Also using an immersion technique, the incidence angle θ_w fixes direction of L and S wave fronts (phase) in the materials and the signals received that are associated with energy (group) are interrelated to the wave fronts by *Eqs 11, 12*. This supports the use of slowness curves s_g as in *Fig. 5*, scanning the phase angle θ_p for representing ultrasonic measurements.

With the objective of recovering stiffness constants from the above expressions, velocity or, more precisely, time-of-flight data are needed for various propagation angles in the material. For that purpose, the sample is insonified by short ultrasonic pulses of center frequency 3 MHz and the time of arrival of the pulses at transducer R are measured. In *Fig. 8*, a ray path representation for the time of flight of either L or S wave is presented for symmetry plane 1–2 or 1–3. As a reference, we will consider the time of flight, t', between T and R in the absence of the sample. Hence, measurements of time of flight, t, are performed with the sample at different angles θ_w after a lateral displacement of transducer R by a distance δ to capture the maximum of the beam energy. The center of the ultrasonic beam is followed by maximizing the envelope of the received signal. In view of *Fig. 8*, the time of flight difference, $t - t'$, can be related to group velocity by the relation:

$$\Delta t = t - t' = \frac{d}{v_g} - \frac{d'}{v_w} \tag{18}$$

or more explicitly, in terms of the sample thickness, e, and the angles θ_w, θ_g as:

$$\frac{v_w}{v_g} = \cos\,\theta_g\left(\cos\,\theta_w + \frac{v_w \Delta t}{e}\right) + \sin\,\theta_g \sin\,\theta_w \tag{19}$$

Also, *Fig. 8* allows one to find an expression for the lateral displacement necessary for detection as:

$$\frac{\delta}{e} = \cos\,\theta_w \tan\,\theta_g - \sin\,\theta_w \tag{20}$$

Equations 19 and *20* are valid either for L or S wave and symmetry plane 1–2 or 1–3, no matter if θ_g is smaller or larger than θ_w. The remaining quantities to be evaluated in order to use the above equations are the sample thickness e and density ρ, which can be obtained in a standard way.

Inversion Algorithm

The above relations are the necessary ingredients for the inverse problem at hand, consisting of recovering the elastic constants from the measurement data. By making sufficient time-of-flight measurements over a range of orientations in the symmetry planes 1–2 and 1–3, one can proceed to optimally recover the stiffness components.

First, measurements in isotropic plane 1–2 should allow to obtain stiffness constants C_{11} and C_{66} according to *Eq 7*. In this plane, propagation of the wave front and energy flux coincide that is, $\theta_g = \theta_p$ and $v_g = v_p$. Therefore, substitution of *Eq 15* into *Eq 19* yields a simple relation between measurement set $\theta_w - \Delta t$ and velocity v_p for either L or S wave in the form:

$$\frac{v_w}{v_p} = \sqrt{1 + 2\,\frac{v_w \Delta t}{e}\cos\,\theta_w + \left(\frac{v_w \Delta t}{e}\right)^2} \tag{21}$$

while the angle θ_p is obtained from *Eq 15*. In addition, for that plane, the measurement set $\theta_w - \Delta t$ in *Eq 21* should give a constant value for v_p independent of propagation direction θ_p. Using the slowness representation for the N measurements at different angles, circular patterns should be obtained for both L and S

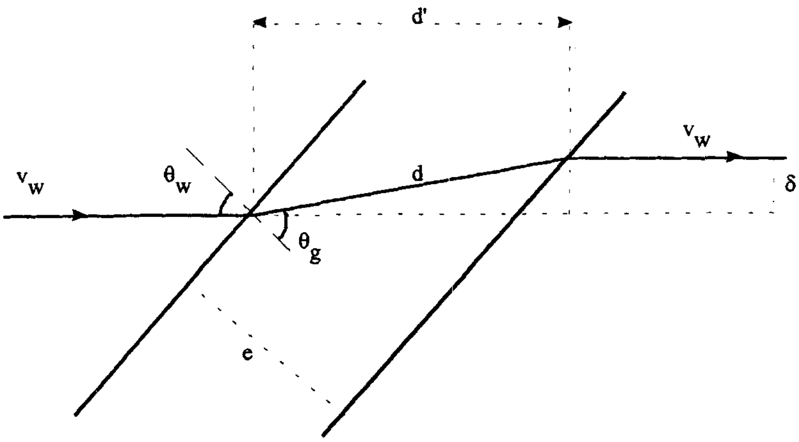

Fig. 8. Ray path representation for time of flight of either L or S wave in symmetry plane 1–2 or 1–3.

modes and therefore allowing validation of the assumption of transversely isotropic symmetry. Once this is verified apart from random deviations, the N measurements at different angles θ_w for each mode are all being used to evaluate the stiffness constants using:

$$C_{11} = \rho \frac{\Sigma(v_p^L)^2}{N} \qquad C_{66} = \rho \frac{\Sigma(v_p^S)^2}{N} \tag{22}$$

Doing this, the relative error, r_v, associated with random noise on the velocities results in an error, r_c, for the stiffness constants C_{11} and C_{66} given by:

$$r_c \approx \frac{2r_v}{\sqrt{N}} \tag{23}$$

Second, measurements in plane 1–3 should allow one to obtain the stiffness constants C_{33}, C_{44}, and C_{13}. The problem is to evaluate the remaining constants from a best-fit of N measurements $\theta_w - \Delta t$ with the above model for propagation. A least-square fit of the N data points to the model consists in minimizing the sum of squares of the deviations between the slownesses of experimental and calculated group velocities, respectively, v_g^e and v_g^c, and making adjustable the unknowns C_{33}, C_{44}, and C_{13}. This can be written as:

$$\min_{C_{33},C_{44},C_{13}} \sum_N \left(\frac{1}{v_g^e} - \frac{1}{v_g^c}\right)^2 \tag{24}$$

where the sum includes measurements from both L and S waves. However, the model described above depends nonlinearly on C_{33}, C_{44}, and C_{13} and therefore, the minimization must proceed iteratively. Given trial values for the parameters, the procedure improves the solution at each iteration and is repeated until *Eq 24* stops decreasing. For this purpose, the downhill simplex method of Nelder and Mead is used here, as being of more general usage and more robust with respect to convergence (13).

Therefore, at each iteration, v_g^c of either L or S modes is computed through the steps of: 1) solving *Eqs 8, 15* for θ_p and v_p given the angle θ_w, 2) computing θ_g from *Eq 12* and 3) evaluating v_g^c from *Eq 10*. Also, the measured time of flight Δt is converted into v_g^e using *Eq 19*. Hence, the sum of *Eq 24* is evaluated and serves as a function of merit for estimating a better trial solution of stiffness constants for the next iteration. We note that due to Snell's law in *Eq 15*, it may happen during the iterative process that the trial solution C_{IJ} prevents the calculation of v_g^c associated with the measurement set $\theta_w - \Delta t$. Since a measurement has actually been performed at this angle, this indicates that the solution C_{IJ} is wrong at the given iteration and has to be changed drastically to allow calculation of v_g^c. Therefore, a penalization technique is proposed where a sufficiently large number associated with the measurement set is introduced in *Eq 24*. This allows the algorithm to improve the solution for the next iteration. Also, the algorithm was found to be generally robust for any reasonable choice of initial parameter set.

The remaining aspect of the problem is the estimation of the errors or uncertainties in obtaining the stiffness constants C_{33}, C_{44}, and C_{13} from N measurements in plane 1–3 using the above procedure. The best way to make these estimates is through Monte Carlo simulation of synthetic data sets (13). The starting point is to consider the parameters obtained from the experimental data set as true and then evaluate the noise level associated with measurements, typically assuming a gaussian white noise distribution. Using computer-generated random numbers, a series of M data sets comprising N points with the same level of noise are simulated as synthetic realizations of the experiment. The above procedure of obtaining the stiffness constants is applied to the M data sets and provided the number M is sufficiently large, calculated standard deviations are good estimates of the uncertainties in obtaining stiffness constants from the experimental set of N points. The relative error for each of the stiffness constants C_{33}, C_{44}, and C_{13} is given by:

$$r_c = \frac{1}{C_0}\sqrt{\frac{1}{M-1}\sum_{m=1}^{M}(C_m - C_0)^2} \tag{25}$$

where C_m is the value obtained from the simulated data set m and C_0 is the true value obtained from the experimental set. A number $M = 100$ was found sufficient for a proper evaluation of the uncertainty in these constants. The method described here for the stiffness constants works equally well for the uncertainties in the engineering constants and is actually used here.

4. MEASUREMENTS ON PET

Roll-Drawing and Process Results

Many efforts have been made in the past two decades on the development of orientation in semicrystalline polymers (1, 14). Particular achievements were made recently on making polyethylene fibers with moduli near 240 GPa (15) using the gel spinning technique. Such highly oriented PE fibers can be used in many applications, as marine ropes and antiballistic clothes. However, because of their low melting temperature and poor creep properties, their use in structural applications is rather limited. In fact, the market is still dominated by composites despite many disadvantages (cost, density, fabrication, recycling). Hence, the potential of oriented polymers obtained by solid state processes in the form of shapes, profiles, and sheets and having properties in the range of those of composites is high.

Experimental results have shown that uniaxial orientation improves stiffness properties in the machine (draw) direction but decreases transverse properties at the same time. Many solutions have been proposed that act on the material and not on the process, therefore limiting their generality. Another solution is biaxial orientation, which requires specific geometrical designs depending on the needed shape. Examples are tubes and flat profiles (16, 17). However, biaxial orientation will limit the maximum draw ratio that can be achieved in comparison to uniaxial deformation. Other solutions, but only for flat profiles, are processes such as rolltrusion, rolling, and roll-drawing.

Many efforts have been directed to materials such as polyethylene (PE) and polypropylene (PP). However, because of their low melting temperatures, as mentioned above for the fibers, their applications are rather limited and particular focus was directed toward polymers with a higher melting point. Some of these studies considered polymers presenting an alpha crystallization temperature, above which intracrystalline interactions are considerably reduced. This permitted the obtainment of draw ratios by solid state deformation >20. Very few studies dealt with semicrystalline polymers that do not present an alpha crystallization, such as PET, nylons, PES, and PEEK (18). For PET, most studies were concerned with its deformation from the melt such as films and fibers. The concern here is on mechanical properties of solid state roll-drawn semicrystalline PET.

In this study, an extrusion grade of PET (Selar PT) purchased from DuPont was used, having a crystallinity of 30% and a melting temperature of 255°C. The PET material was first dried at 120°C before being fed to the extruder. The feed zone temperature of the extruder was set between 240 and 260°C, the following zones, temperatures were between 260 and 290°C and the die zone temperature between 265 and 280°C. The temperatures in the gear pump section were set between 270 and 280°C. The extruder PM and resulting pressure depended on the output used. The extruder's output profile speed was between 20 and 100 cm/min. The deformation temperature ranged from 180 to 230°C. The initial profile dimensions were 1 cm in thickness and 10 cm in width. The isotropic profiles were marked regularly before entry into the rolls by 10 cm spaced lines. The draw ratio was calculated using these marks, corresponding in fact to the length draw ratio.

The roll-drawing equipment consisted of a series of four pairs of rolls, with adjustable speed and temperature. In order to minimize relaxation and elastic recovery effects, the profile has to be maintained under tension after the deformation by rolling. By application of tension as reported previously (18), it was possible to achieve a maximum draw ratio of 5.2 for PET, under normal cooling conditions (ambient air) and for rolls gap of 1.25 mm. The initial PET profile crystallinity of 30% was found to increase with draw ratio, attaining 50% for a draw ratio of 5. This induced a small change in the density from 1380 to 1408 kg/m^3, a variation of ±1%.

Ultrasonic Results and Discussion

Ultrasonic mapping of anisotropy and evaluation of stiffness constants can now be made on oriented samples of PET with the procedure described in the previous section. Using an immersion technique, time-of-flight measurements in various directions of the material will allow us to determine the different stiffness components. Samples were cut from the flat profiles obtained with draw ratios from 1.0 to 4.2. The thicknesses, e, were measured and found between 2 and 9 mm. For the density, a constant value $\rho = 1400$ kg/m^3 is used in the calculation. Also, measurements at different angles in the transverse plane will allow direct validation of the approximation for transversely isotropic symmetry. From the waveform data, the only information required is time-of-flight differences Δt of L and S modes, that for different angles θ_w not necessarily at fixed interval. A best fit with respect to group velocity using *Eqs 22, 24* is obtained on each sample with different draw ratios simultaneously using the data for both L and S modes.

As an example, the time-of-flight data and the best fit obtained for the sample with a draw ratio $\lambda = 2.23$ is shown in *Fig. 9*. In *Fig. 9a*, the time-of-flight differences Δt normalized with v_w/e are shown for both L and S modes for different angles θ_w in planes 1–2 (squares) and 1–3 (circles). As expected, the arrivals in these planes are different. One first notices the presence of L mode for angle $\theta_w < 40°$ in plane 1–2 while it is only for $\theta_w < 30°$ in plane 1–3. For S mode, the pulse arrivals are clearly different in plane 1–2 compared to plane 1–3. Correspondingly, in *Fig. 9b*, the best fit obtained with group velocity is excellent with the elastic constants as given in *Table 2* together with the uncertainties. One notices that Young's moduli are clearly different along axes 1 and 3 with a ratio $E_3/E_1 = 2.1$. Also, such polar plots of the slowness $1/v_g$ vs. θ_p for L and S modes in symmetry planes 1–2 and 1–3 allow a detailed mapping of the anisotropy in the material. An important point is the circular patterns observed for plane 1–2 in this *Figure*, which validate the assumption of transversely isotropic symmetry. Similar good fits were obtained for all PET samples with uncertainties on the stiffness and engineering constants of <5%.

Figure 10 illustrates for plane 1–3 an example of necessary lateral displacement, δ, for transducer R in order to follow the center of ultrasonic beam with maximum amplitude and acquire the appropriate time of flight data. Measurement data in *Fig. 10* are for L and S modes and predictions from the model (with stiffness constants already evaluated) are shown for the wave front (dotted lines) and energy flux (solid lines). As clearly shown in this *Figure*, detection of an ultrasonic signal appears more related to energy propagation (group velocity) than to wave front propagation (phase velocity). This is especially convincing in view of the widely different behaviors associated with the S mode.

In *Figs. 11* and *12*, all seven engineering constants for the different PET samples are presented as a function of draw ratio λ. *Figures 11a* and *11b* show the results, respectively, for the axial and transverse Young's moduli. In parallel to using ultrasonics for

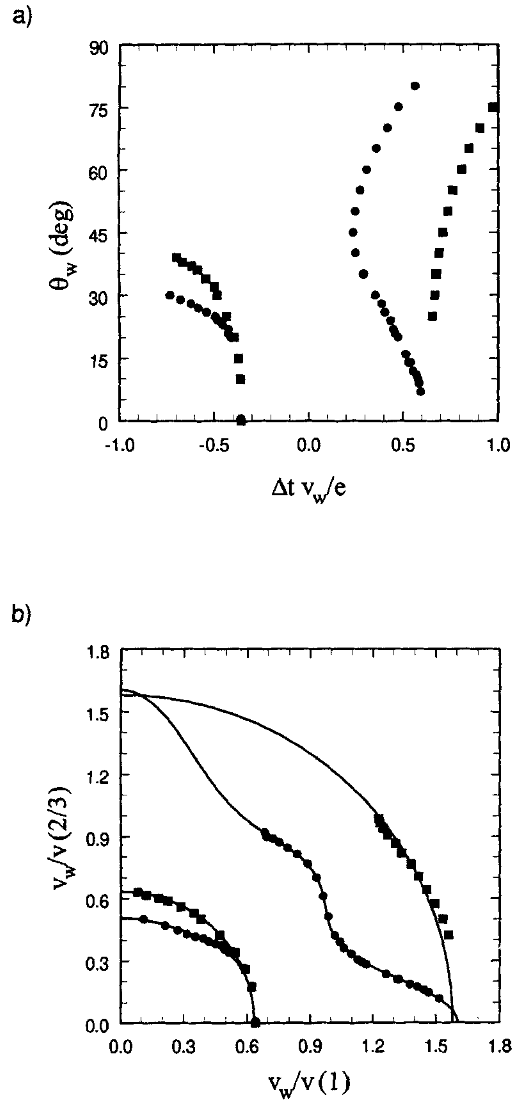

Fig. 9. Results for the PET sample with draw ratio $\lambda = 2.23$ in planes 1–2 (squares) and 1–3 (circles): a) time-of-flight measurements and b) corresponding best fit with group velocity representing the anisotropy in the sample.

Table 2. Elastic Constants Corresponding to Best Fit for a PET Sample With Draw Ratio λ = 2.23.

Stiffness Constants		Engineering Constants	
C_{11}	7.68 GPa ± 1.0%	E_3	8.14 GPa ± 1.0%
C_{66}	1.24 GPa ± 1.0%	E_1	3.85 GPa ± 1.0%
C_{33}	12.11 GPa ± 1.0%	G_{13}	1.20 GPa ± 2.0%
C_{44}	1.20 GPa ± 2.0%	G_{12}	1.24 GPa ± 1.0%
C_{13}	5.06 GPa ± 1.0%	ν_{13}	0.39 ± 1.0%
		ν_{12}	0.56 ± 1.0%
		ν_{31}	0.19 ± 2.0%

assessing stiffness constants, results from static tensile tests are also presented in these *Figures*. With this range of draw ratio for PET, the axial modulus determined by ultrasonics increases almost linearly from 4 to 16 GPa while the transverse modulus is almost constant near 4 GPa. This proves the efficiency of the roll-drawing process for flat profiles to improve stiffness properties in the machine direction without deteriorating transverse properties, as compared with uniaxial deformation.

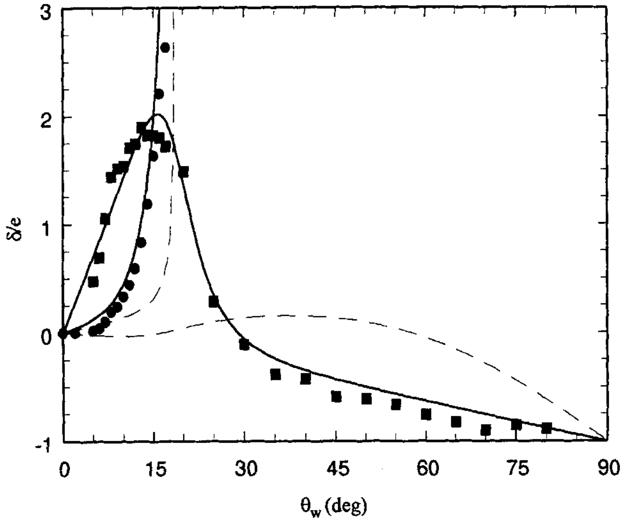

Fig. 10. Lateral displacement for transducer R in plane 1–3. Measurements are for both L (circles) and S (squares) modes; predictions from the model are for wave front (dotted lines) and energy flux (solid lines).

For comparison, moduli obtained from mechanical tensile tests show the same tendency with draw ratio, but with values always lower than those determined using ultrasonics. For the axial modulus, the deviation increases progressively with the draw ratio from 20% to 60% while the transverse modulus remains roughly constant around 15%. In fact, these results for the semicrystalline PET can be interpreted in terms of the viscoelasticity associated with the amorphous and crystalline phases. While mechanical tests are performed at low frequency, typically 1–10 Hz, ultrasonic moduli correspond to frequencies in the MHz range. In terms of time-temperature equivalence principle, this means that the ultrasonic results obtained at or near 20°C should be compared with static measurements at or near −40°C (2, 3). Therefore, increasing the draw ratio, the crystalline and amorphous components are made more aligned and parallel to the draw axis with a stronger viscoelastic behavior. In the transverse direction, low forces of Van der Waals and hydrogen bonding types are being more involved compared with the isotropic material, hence limiting the effect due to viscoelasticity.

In *Figs. 12a* and *12b*, results are shown, respectively, for the two shear moduli and the three Poisson's ratios as determined by ultrasonics. With this range of draw ratio in *Fig. 12a*, the modulus G_{12} is shown to continuously decrease from 1.5 to 1.2 GPa. For the modulus G_{13} however, the decrease is found more drastic, from 1.5 to 0.9 GPa (40%) and only upon exceeding a draw ratio of $\lambda = 2$. Here, two different reasons may explain this effect. The first reason would be the sensitivity of modulus G_{13} to the sliding of lamellae and the presence of dislocations by further

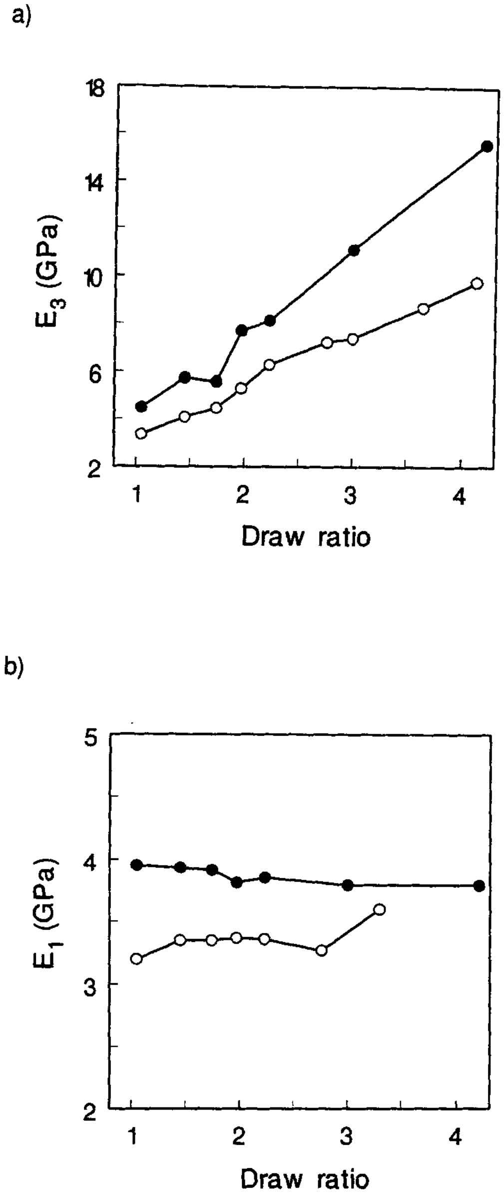

Fig. 11. Draw ratio dependence for Young's moduli of PET samples. Results are from ultrasonics (solid circles) and static tests (empty circles) for a) axial modulus and b) transverse modulus.

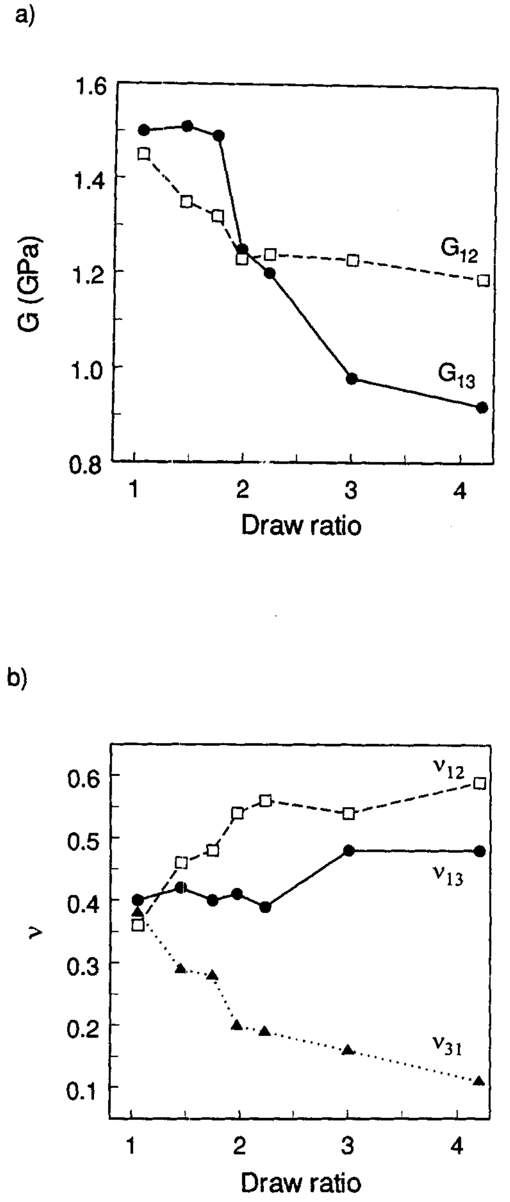

Fig. 12. Draw ratio dependence for a) shear moduli and b) Poisson's ratios of PET samples as obtained from ultrasonics.

increasing the draw ratio above $\lambda = 2$ for PET. The second would be the later alignment of the amorphous phase yielding the low forces in the transverse direction as above and the greater ease for splitting along planes 1–3. For Poisson's ratios in *Fig. 12b* with this range of draw ratio, ν_{31} is found to continuously decrease as expected from 0.38 to 0.11 while ν_{13} is only slightly increasing from 0.40 to 0.48. For the case of ν_{12}, however, the increase is more pronounced, from 0.36 to 0.59 (60%), but occurs mainly in the range of the low draw ratios (up to $\lambda = 2$). We believe this Poisson's ratio is dominated by the alignment of the crystalline phase occurring in the first stage. In all cases, values of Poisson's ratios obtained by ultrasonics fall within the bounds derived in the literature for anisotropic materials (19, 20).

5. CONCLUSION

We have shown that ultrasonics is a useful method for investigating the elastic properties as well as characterizing the anisotropy of oriented polymers, in particular roll-drawn PET. While being nondestructive, such a method allows the determination of more mechanical moduli with a better accuracy than conventional tensile methods, especially regarding shear properties. An improved version of the immersion technique is proposed in this work using a formalism based on the group velocity for analyzing time-of-flight data, including the allowance for lateral displacement of the transmitted beam. We have shown an example of lateral displacement which clearly indicates that ultrasonic signal detected relates to energy propagation (group velocity), not to wave front (phase velocity). We have also outlined a robust algorithm for the recovery of elastic constants from experimental time-of-flight data.

Results are presented for the roll-drawing of PET with various draw ratios. Here, the main results for roll-drawn PET are summarized as followed: 1) the circular patterns observed for plane 1–2 validate the assumption of transversely isotropic symmetry for draw ratios up to 4.2, 2) the efficiency of the roll-drawing process for flat profiles is proven, improving stiffness properties in the machine direction without decreasing transverse properties, 3) the larger ultrasonic Young's moduli by 10% to 60% comparing with tensile tests can be interpreted in terms of viscoelasticity considering both the amorphous and crystalline phases, 4) the 40% decrease of shear modulus G_{13} upon exceeding a draw ratio of 2 may be explained by the lamellae sliding and the later alignment of the amorphous phase and 5) the 60% increase of Poisson's ratio ν_{12} attaining 0.59 for low draw ratios is due to the alignment of the crystalline phase in the first stage.

REFERENCES

1. I. M. Ward, in *Mechanical Properties of Solid Polymers*, 2nd Ed., Wiley-Interscience Publication, England (1983).
2. W. P. Leung, C. C. Chan, F. C. Chen, and C. L. Choy, *Polymer*, **21,** 1148 (1980).
3. C. L. Choy and W. P. Leung, *J. Polym. Sci.: Polym. Phys. Ed.*, **23,** 1759 (1985).
4. S. I. Rokhlin and W. Wang, *J. Acoust. Soc. Am.*, **91,** 3303 (1992).
5. S. R. A. Dyer, D. Lord, I. J. Hutchinson, I. M. Ward, and R. A. Duckett, *J. Phys. D: Appl. Phys.*, **25,** 66 (1992).
6. B. Castagnede, K. Y. Kim, W. Sachse, and M. O. Thompson, *J. Appl. Phys.*, **70,** 150 (1991).
7. A. G. Every and W. Sachse, *Phys. Rev. B*, **42,** 8196 (1990).
8. L. P. Scudder, D. A. Hutchins, and J. T. Mottram, *Ultrasonics*, **32,** 347 (1994).
9. K. Y. Kim, *Phys. Rev. B*, **49,** 3713 (1994).
10. Y. C. Chu and S. I. Rokhlin, *J. Acoust. Soc. Am.*, **95,** 213 (1994).
11. M. J. P. Musgrave, *Crystal Acoustics*, Holden-Day, London (1970).
12. S. C. Wooh and I. M. Daniel, *J. Acoust. Soc. Am.*, **90,** 3248 (1991).
13. W. H. Press, S. A. Teukolsky, W. T. Vetterling, and B. P. Flannery, *Numerical Recipes in Fortran*, Cambridge Univ. Press, New York (1992).
14. I. M. Ward, *Adv. Polym. Sci.*, **70,** 1 (1985).
15. R. S. Porter, T. Kanamoto, and A. E. Zachariades, *Polymer*, **35,** 4979 (1994).
16. S. J. Pan, H. I. Tang, A. Hiltner, and E. Baer, *Polym. Eng. Sci.*, **27,** 869 (1987).
17. L. Mascia and J. Zhao, *Rheol. Acta*, **30,** 369 (1991).
18. A. Ajji, J. Dufour, N. Legros, and M. M. Dumoulin, *J. Reinf. Plast. Comp.*, **15,** 652 (1996).
19. R. M. Christensen, *Mechanics of Composite Materials*, p. 79, John Wiley, New York (1979).
20. R. M. Jones, *Mechanics of Composite Materials*, pp. 42–44, McGraw-Hill, New York (1975).